Computational Investigation of the Effect of Chemistry on Mars Supersonic Retropropulsion Environments

Gabriel Nastac*, Ashley Korzun†, Aaron Walden‡, Eric Nielsen§, and William Jones¶
NASA Langley Research Center, Hampton, Virginia, 23681

Patrick Moran‖
NASA Ames Research Center, Moffett Field, California, 94035

Retropropulsion ground tests require significant compromises on physical scale, instrumentation, configuration, and environments. Matching the full Martian environment is simply not possible on Earth. Ground tests of retropropulsion configurations thus far have neglected effects of chemistry due to physical constraints of wind tunnel models and facilities; most experiments use inert simulant gases at relatively low temperatures. As such, a strong reliance on high-fidelity computational analyses is required to expand the knowledge of retropropulsion aerodynamics. In this work, we investigate the effects of chemistry using scale-resolving computational fluid dynamics (CFD) with finite-rate chemistry and a graphics processing unit (GPU)-enabled implementation of the NASA FUN3D flow solver on a human-scale Mars lander concept at supersonic freestream conditions. Results are compared to previous perfect gas simulations.

I. Introduction

Human-scale Mars atmospheric entry missions require an order of magnitude increase in payload capability compared to past missions [1]. Entry, descent, and landing (EDL) concepts consequently require complex retropropulsion strategies [2] to successfully land payloads. There have been several experiments in past decades investigating supersonic retropropulsion (SRP) flows. Most experiments however, due to the physical constraints of simulating realistic rocket engines at wind tunnel scale, primarily utilize perfect gases [2]. There is a general gap in the understanding of the effects of chemistry in these flows. Exhausting combustion products into the shock layer increases heat transfer for the liquid oxygen and methane engines planned for human Mars missions. During the powered descent phase, these human-scale landers travel through the atmosphere as well as the engine exhaust, so understanding the exhaust gas is vital to design and fly these next generation vehicles. In addition, experiments have shown oscillatory and unstable flow behaviors; an understanding of these phenomena is necessary to reliably predict these flows for vehicle stability and control.

The primary simulation methodology during the last decade for SRP flows has been perfect gas steady-state computational fluid dynamics (CFD) simulations [2]. For example, Ref. [3] simulates air experiments using the NASA OVERFLOW, DPLR, and FUN3D flow solvers using perfect gas assumptions and steady-state, 3-D Reynolds-averaged Navier-Stokes (RANS) with reasonable agreement to each other and with the experimental data. Continuing work in Ref. [4] simulated more recent experiments [5] using unsteady methods, including detached-eddy simulation (DES) and unsteady RANS (URANS) using the same three flow solvers with generally favorable agreement to the experiments. Reference [6] numerically investigated the effects of SRP on recent inert gas experiments done at the University of Virginia at hypersonic freestream Mach numbers using axisymmetric steady-state simulations. There are three main limitations in this study [6]: the freestream enthalpy levels are approximately two orders of magnitude smaller than Mars atmospheric entry; chemistry is neglected (both in the thrusters and in the atmosphere); and turbulence is neglected. Reference [7] investigated the effects of chemistry on capsule reaction control systems (RCS) using axisymmetric and semisymmetric 3-D steady-state simulations. Reference [8] simulated an SRP descent of the Falcon 9 using four CFD solvers, including FUN3D, using RANS with frozen and perfect gas species, a common methodology to simulate these

*Research Scientist, AIAA Member
†Research Aerospace Engineer, AIAA Senior Member
‡Research Scientist
§Senior Research Scientist, AIAA Associate Fellow
¶Computer Scientist, AIAA Associate Fellow
‖Computer Scientist

flows. In general, the CFD solvers predict total forces and moments that favorably match the available flight data across most of the trajectory investigated. Reference [9] also simulated an SRP descent of a launch vehicle using the DLR TAU flow solver. One simulation in their matrix used finite-rate chemistry, with the rest being two perfect gas species RANS simulations. The one finite-rate chemistry simulation predicted a temperature increase of roughly 1000 K around the vehicle base. Later simulations by the same group [10] simulated a similar setup using Spalart-Allmaras DES (SA DES) [11] with the two perfect gas species approach.

Past work by the authors [12] involved simulations of a human-scale Mars lander concept based on upcoming perfect gas air experiments [13]. FUN3D was used to simulate the lander concept on the GPU-based Summit supercomputer [14], a U.S. Department of Energy resource located at the Oak Ridge Leadership Computing Facility [12]. Solution ensembles were performed to investigate the effects of spatial resolution, freestream Mach number, and engine throttle settings on the vehicle's resulting aerodynamics. Spatial domains were large enough to be measured in units of kilometers, and flow features on the scale of centimeters were resolved in the simulations.

Physically realistic CFD simulations of SRP flows require unsteady chemistry models and are computationally expensive. Current state-of-the-art for chemically reacting SRP flows is 2-D, axisymmetric, and 3-D steady-state simulations. Current practice is to use two perfect gas species, with one species representing the engine exhaust products and another representing the freestream or atmosphere, neglecting post-chamber reactions. These practices are in large part due to impractical computational time and cost. One wall-resolved perfect gas unsteady simulation of SRP for a few seconds of physical time with one billion degrees of freedom takes about three months on 5,000 high-end CPU cores [12]. A 10-species reacting gas simulation is over ten times more expensive than a perfect gas simulation on the same computational grid, which implies a total simulation time of about two and a half years on those same 5,000 CPU cores. For design and analyses of these flows and vehicles, hundreds of simulations must be run. As such, efforts must be pursued to reduce time-to-solution for these complex flows, specifically in the area of high-fidelity CFD on emerging supercomputing architectures.

Current plans for U.S. exascale systems [15–17] all rely on GPU acceleration to achieve exascale performance. The NASA CFD Vision 2030 and CFD2030 Grand Challenge studies [18, 19] emphasize the need for effective utilization of this next generation hardware to achieve the simulation goals of the aerospace community. An efficient and scalable GPU-enabled modeling approach was developed for this work [20]. This approach is currently being applied to run simulations at scale on Summit, using over half of the machine to simulate these flows using billions of elements with finite-rate chemistry solved with implicit time stepping to enable realistic trajectory temporal integration times (on the order of several physical seconds) while resolving the turbulent boundary layer of the vehicle. As demonstrated in experiments and simulations, SRP flows have oscillatory and unstable flow behaviors that cannot be accurately predicted using steady-state methods. There are thus general gaps in understanding the effects of finite-rate chemistry on these flows as well as in the importance and impact of scale-resolved simulations, which have been shown to be necessary for combustion problems in other fields [21].

The ability to properly simulate thermodynamic and transport properties of both the Martian atmosphere and the high-enthalpy rocket exhaust is critical for accurate prediction of retropropulsion-induced environments on the vehicle. The obstruction ahead of the vehicle created by retropropulsion governs the magnitude and behavior of aerodynamic variations on the vehicle. The flowfield structure defining this obstruction is highly dependent on the expansions, shocks, shear layers, and mixing interfaces comprising it. The conditions, including pressure, temperature, and specific heat capacity, are strong functions of the chemical composition of the local fluid mixture. This work aims to computationally investigate the effects of chemistry on a Mars lander concept. Specifically, the past campaign [12] is currently being revisited with finite-rate chemistry. An overview of the current campaign focused on chemistry is detailed in Ref. [22]. To maintain some form of dynamic similitude, various key parameters such as Mach number, Reynolds number, nozzle exit-to-stagnation freestream pressure ratios, nozzle exit Mach number, and dynamic pressure were matched for conditions along a proposed descent trajectory. By matching these parameters, the general flow features depicted in Fig. 1 will, in theory, be similar. Understanding the effects of chemistry for these flows and the impact on general plume shapes (extents, widths, and shear layer thicknesses), jet terminal shock shape and size, recirculation regions near plumes and between the detached bow shock and jet terminal shock, detached bow shock standoff distance, and aerodynamic and propulsive forces and moments are important for eventual vehicle design. Spatial chemical composition is of interest to determine the extent of reactions beyond the jet terminal shock. Temperature and chemical composition near the surface of the vehicle are also of importance for heat transfer and thermal protection system response prediction.

Since some of these parameters are primarily derived from perfect gas theory, similarity is not necessarily possible. For example, nozzle exit pressure is a function of chemical composition. For perfect gas flows, it is possible to obtain a theoretical 1-D estimate for this since specific heat ratio is fixed, but with varying chemistry in addition to realistic,

nonideal nozzles, estimating a nominal exit pressure is not possible with theory since the nozzle flow will be neither frozen nor in equilibrium. Other variables are matched more easily.

The following sections first describe the methodology, including governing equations and numerical implementation. The supersonic condition of the current simulation campaign is then described for both air (once again, to match experimental setup) and realistic Martian conditions. Results for the human-scale Mars lander concept are then presented and compared between the two methods. Throttle conditions are also varied to investigate their effects on vehicle performance and flowfields; specifically, 80% and 60% engine throttle conditions are examined. The higher thrust condition leads to underexpanded plumes, whereas the lower thrust condition leads to overexpanded plumes.

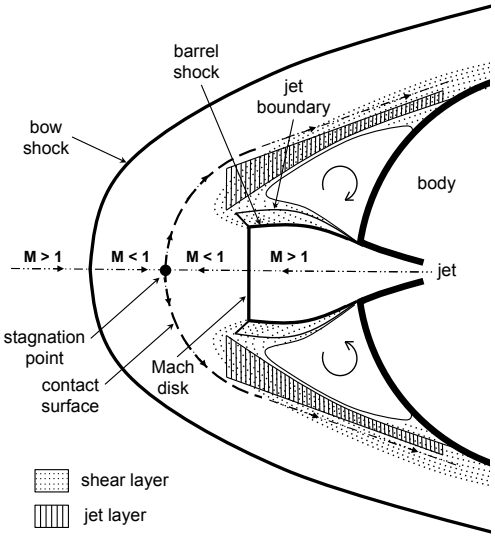


Fig. 1 Characteristic flow field for supersonic retropropulsion (adapted from [2]).

II. Methodology

A. Governing Equations and Numerical Implementation

The governing equations for compressible reacting flow are the conservation of species, mixture momentum, and total energy:

$$\frac{\partial}{\partial t}\left(\rho y_s\right) + \frac{\partial}{\partial x_j}\left(\rho y_s u_j\right) - \frac{\partial}{\partial x_j}\left(J_{sj}\right) = \dot{\omega}_s, \tag{1}$$

$$\frac{\partial}{\partial t}\left(\rho u_i\right) + \frac{\partial}{\partial x_j}\left(\rho u_i u_j + p\delta_{ij}\right) - \frac{\partial}{\partial x_j}\left(\tau_{ij}\right) = 0, \tag{2}$$

$$\frac{\partial}{\partial t}\left(\rho E\right) + \frac{\partial}{\partial x_j}\left(\left(\rho E + p\right) u_j\right) - \frac{\partial}{\partial x_j}\left(u_k \tau_{kj} + \dot{q}_j + \sum_{s=1}^{N_s} h_s J_{sj}\right) = 0, \tag{3}$$

where y_s is the mass fraction of species s, $\rho = \sum_{s=1}^{N_s} \rho y_s$ is the mixture density, $\rho_s = \rho y_s$ is the species density of species s, u_i is the ith component of the velocity, and E is the total energy. J_{sj} is the jth component of the diffusive flux, $\dot{\omega}_s$ is the chemical source term of species s, p is the pressure, τ_{ij} is the shear-stress tensor, $\dot{q}_j$ is the jth component of the heat flux, and h_s is the enthalpy of species s. Pressure is modeled as an ideal gas, heat transfer is modeled with Fourier's law, species diffusion is modeled using Fick's law, and the shear-stress is modeled with a Newtonian model. NASA polynomials [23] are used to compute thermodynamic properties on a per-species basis. The transport properties (diffusivity, viscosity, and thermal conductivity) are computed using collision integrals [24]. The compressible perfect gas equations can be obtained by assuming a single perfect gas species with thermally perfect thermodynamic properties and simplified transport properties (e.g., constant Prandtl number and Sutherland's law).

The governing equations are solved using FUN3D, an unstructured grid node-based finite-volume CFD solver developed at the NASA Langley Research Center [25]. A median-dual finite-volume approach is used for spatial discretization on generic unstructured grids containing tetrahedra, pyramids, prisms, and hexahedra. A dual-grid is generated by bisecting every edge and connecting with cell centroids to generate polyhedra. Inviscid fluxes are computed at each dual-face using an approximate Riemann solver, Roe scheme [26] in this work, with second-order accuracy obtained using an unstructured Monotonic Upstream-centered Scheme for Conservation Laws (MUSCL) reconstruction [27, 28] with unweighted least-squares gradients. In this work, the van Albada flux limiter [28] is utilized for MUSCL [28]. Viscous fluxes are computed using Green-Gauss element-based gradients, equivalent to a Galerkin-based approach for tetrahedra. The equations are integrated in time using an implicit formulation. For the thermochemical nonequilibrium path of FUN3D, turbulence and chemistry are solved fully coupled with momentum and energy.

Turbulence for the previous perfect gas campaign is modeled using Spalart-Allmaras DES [11] and solved with a decoupled methodology. For the finite-rate chemistry campaign, turbulence is modeled using SA-Catris DES [11, 29] and solved with a fully coupled methodology. A comparison of these models including unsteady Reynolds-averaged Navier-Stokes (URANS) on a single engine supersonic retropropulsion flow [5] is presented in the appendix. The two DES variants produce comparable results for the configuration investigated.

FUN3D is implemented in Modern Fortran and CUDA C++. This work primarily utilizes a standalone CUDA C++ library of FUN3D kernels called FLUDA, which enables the usage of NVIDIA GPU architectures [20]. This recent work has shown performance improvements for the thermochemical nonequilibrium path of more than an order of magnitude for an NVIDIA Tesla V100 over a typical x86 CPU node consisting of 40 physical cores, with the caveat that the CPU implementation is suboptimal. Specifically, some optimizations have not been performed and templates are not available in the Fortran implementation, which are important for performance when solving an arbitrary number of partial differential equations (PDEs). The details on the governing equations as well as numerical and software implementation can be found in Refs. [20, 24].

B. Computational Campaign

The simulations of the Mars lander with finite-rate chemistry are part of a current campaign using Summit at Oak Ridge National Laboratory (ORNL) [14]. The objectives of the current campaign and study are to assess the effects of chemistry for retropropulsion in the Mars atmosphere during EDL, quantifying differences in flowfield structures, unsteady behavior, and vehicle aerodynamic forces and moments compared to previous perfect gas studies [12, 30]. This work aims to quantify limitations of prior scaling assumptions and past wind tunnel tests. Another objective of this work is to demonstrate the ability of a thermochemical nonequilibrium CFD solver to effectively utilize GPU-enabled hardware similar to that of upcoming exascale supercomputers.

The perfect gas campaign was aligned with perfect gas experiments scheduled for execution in early 2022 at NASA [13]. The concept is a low-L/D human-scale Mars lander with eight identical rocket engines and a heatshield diameter of 16.4 meters [1]. The vehicle geometry, retropropulsion configuration, and coordinate systems are shown in Figs. 2 and 3. The perfect gas campaign was scaled from Mars-relevant conditions. For example, the nozzles' unscarfed exit-to-throat area ratio was scaled from 177:1 to 35:1 to match the exit Mach number and pressure using air instead of oxygen-methane combustion products. Since the current work simulates the problem with finite-rate chemistry, the nominal engine geometries are utilized here. Various conditions along a proposed descent trajectory from supersonic speeds to transonic speeds are simulated. In this work, we focus on the supersonic conditions at Mach 2.4. Other conditions are examined in Ref. [22]. Freestream Mach number, Reynolds number, dynamic pressure, exit nozzle pressure-to-freestream post-shock stagnation pressure, and exit nozzle Mach number are matched between the finite-rate chemistry and perfect gas simulations. The primary difference between the two campaigns is chemical composition and reactions.

Grids are generated with GridEx [31] and AFLR3 [32]. Grids consist of prismatic boundary layers (fully resolving the turbulent boundary layer with normal wall spacing targeting a $y^+ \approx 1$) near the surface and nearly isotropic (sources are prescribed as isotropic) tetrahedra everywhere else, with pyramids as necessary at the interfaces. Identical volume grid sources are used from the previous campaign, with the main differences primarily relating to nozzle geometry. Surface and volume grids are shown in Figs. 4 and 5, respectively. The largest grid generated through conventional meshing in this work is 139 million points. The grid is then bisected at each edge to generate a finer grid with approximately eight times as many points. New points generated on the surfaces are projected back onto the original analytical CAD definition followed by a linear elasticity procedure [33] to propagate the updated node positions into the interior. More details on gridding strategies and wall spacings are detailed in Ref. [12].

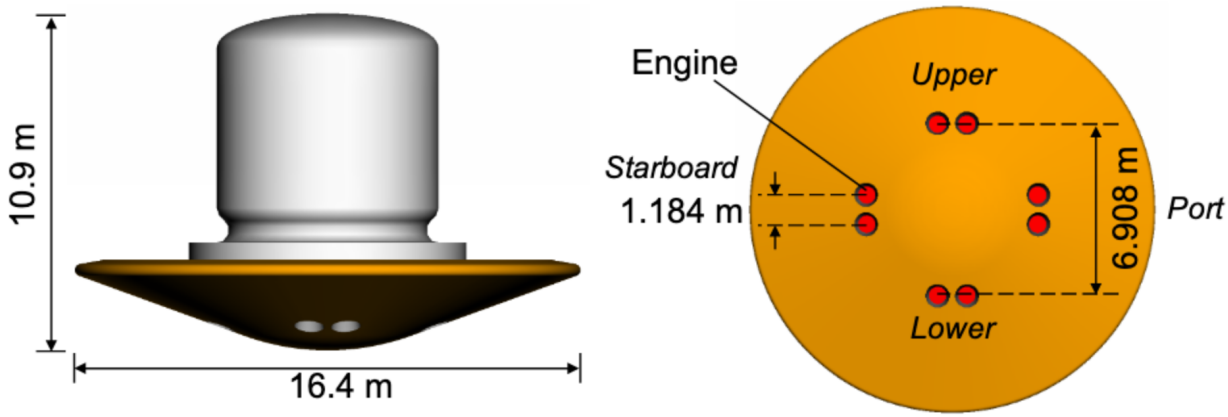


Fig. 2 Vehicle geometry and retropropulsion configuration.

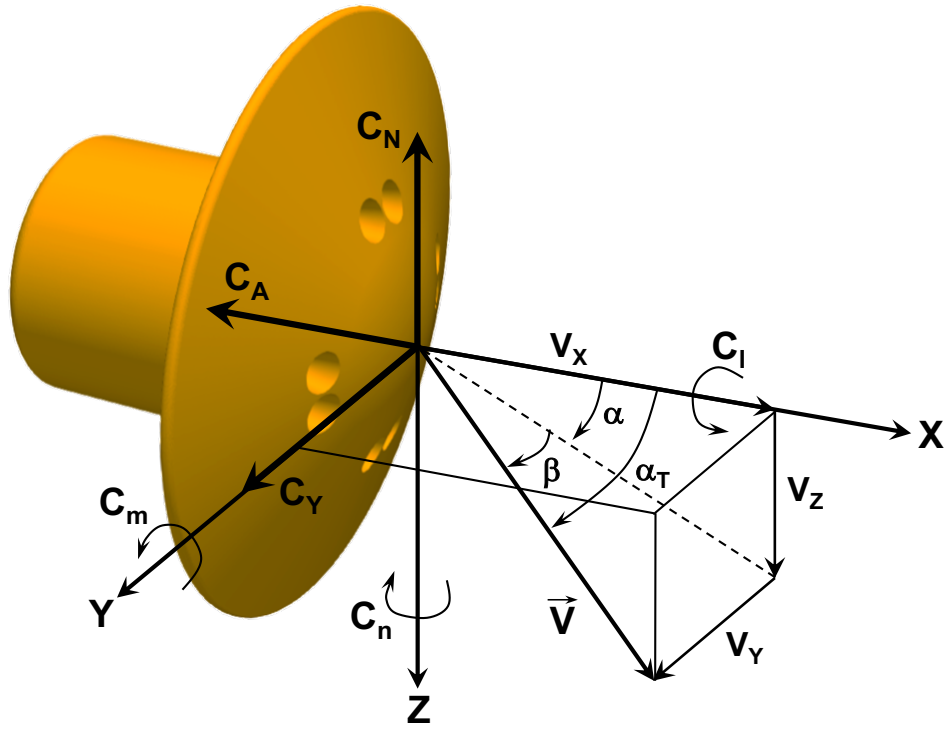


Fig. 3 Vehicle coordinate system.

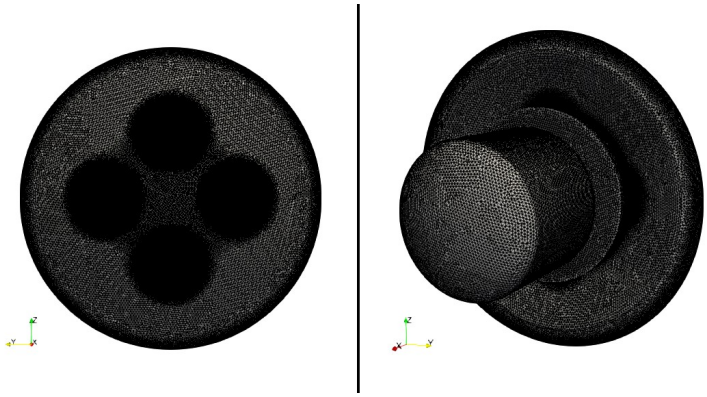


Fig. 4 Surface for 139 million point grid.

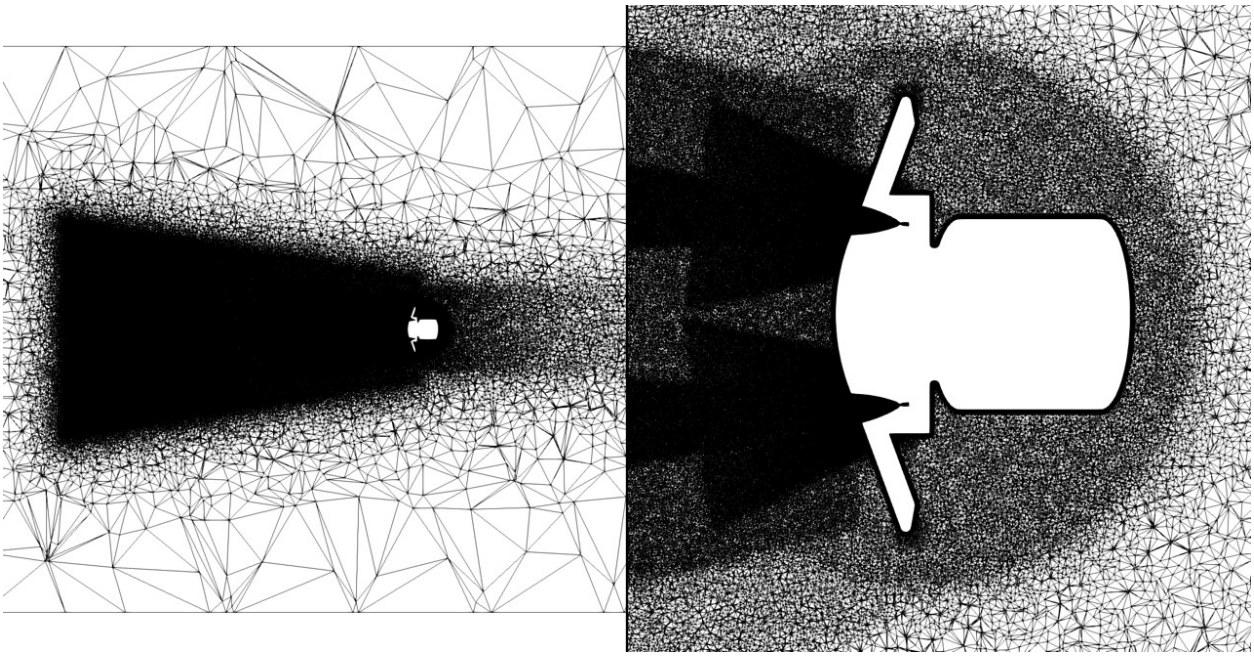


Fig. 5 Volume slice for 139 million point grid.

III. Supersonic Retropropulsion Flow for a Human-Scale Mars Lander Concept

The freestream Mach number and Reynolds number are set to match previous perfect gas simulations [12], nominally $M_\infty = 2.4$ and $Re_D \approx 5.9 \times 10^6$, where D is the heatshield diameter, 16.4 m. The freestream velocity, temperature, and density are 560.6 m/s, 216.53 K, and 0.007 kg/m^3, respectively. The Martian atmosphere freestream is set to 97% CO_2 and 3% N_2 by mass. A 10-species, 19-reaction chemical mechanism is utilized with a one-temperature model. The species used are: CO_2, N_2, C, O, H_2O, H_2, CO, OH, O_2, and H. The set of 19 reactions are shown in Table 1, where M is used to represent a third body. An equilibrium composition of the products of methane-oxygen combustion, with an oxidizer-to-fuel ratio of 3.5, is used for the eight nozzle plena with a total temperature of 3582 K (see Table 2). Two thrust conditions are investigated which correspond to the A.1 (all eight engines at 80% throttle) and A.5 (all eight engines at 60% throttle) conditions from the previous campaign [12]. The total pressure for the engines vary based on the throttle conditions examined: for 80% throttle, the nominal thrust condition, the total pressure for the engines is set to 84.46 bar. For 60% throttle, the total pressure for the engines is set to 63.34 bar. The walls are modeled as no slip adiabatic, noncatalytic walls for consistency with previous perfect gas runs. The thickness of the turbulent boundary

layer, δ_{99}, at the nozzle exits is approximately 8% of the exit nozzle radius (see Fig. 6). In total, there are 15 partial differential equations for the system.

The supersonic condition is run using two grid levels. The coarse grid consists of 139,032,353 points and 737,978,861 cells (692,973,657 tetrahedra, 44,945,072 prisms, and 60,132 pyramids). The fine grid consists of 1,106,828,365 points and 5,903,951,152 cells (5,544,029,784 tetrahedra, 359,560,576 prisms, and 360,792 pyramids). The fine grid is run using 922 Summit nodes (5,532 NVIDIA Tesla V100s) for the 80% throttle condition and 2317 Summit nodes (13,902 NVIDIA Tesla V100s) for the 60% throttle condition. The physical time step is 8.56 μs, which is approximately 3400 time steps per reference time based on the heatshield diameter, $\tau = D/u_\infty$. The convective CFL number upstream of the vehicle is of order unity, and the global convective CFL number, neglecting effects of chemistry, which imposes further restrictions, is approximately 225 based on the plena wall conditions. The fine grid simulations are initialized from interpolated coarser grid solutions. Nominally for the campaign, three hundred thousand time steps (88 τ) are run. In this work, the fine grid with engines at 80% throttle is run an additional two hundred and twenty thousand time steps (64 τ) for improved statistics. The 60% throttle cases are run two hundred thousand time steps (59 τ). Temporal averaging is performed starting from one hundred thousand time steps, after initial transients have passed, and continues to the end of the runs. Five subiterations are used per time step, achieving 3-4 orders of magnitude reduction in residual for species, momentum, energy, and turbulence equations. In total, the nominal physical integration time is about 2.5 seconds. The mean computational cost per time step for the fine grid is 1.18 seconds for 922 Summit nodes and 0.62 seconds for 2317 Summit nodes, leading to total simulation runtimes for 2.5 physical seconds of 100 hours and 50 hours, respectively. Twenty variables (species densities, density, velocity, pressure, temperature, turbulence variable, dynamic viscosity, vorticity magnitude, and Mach number) are saved for the entire volume (90+ GB) every 50 time steps. Asynchronous I/O is utilized, which has a less than 1% overhead on the runtime cost. One run generates about 600 TB of data. The following section will discuss the simulation results concerning the overall flowfield and engineering quantities of interest.

Table 1 Chemical mechanism used for this study. Units are in seconds, moles, cubic centimeters, calories, and Kelvin. [a] Rate coefficients are given in the form $k = AT^n e^{-T_a/T}$.

#	Reaction[a]	A	n	T_a	Factors and Reference
1	$CO + M \longleftrightarrow C + O + M$	1.2×10^{21}	−1.0	1.29×10^5	H, C, O = 1.5, [34]
2	$CO + O \longleftrightarrow O_2 + C$	3.9×10^{13}	−0.18	6.92×10^4	[35]
3	$CO_2 + M \longleftrightarrow CO + O + M$	6.9×10^{21}	−1.5	6.3275×10^4	H, C, O = 2.0, [35]
4	$CO_2 + O \longleftrightarrow O_2 + CO$	2.7×10^{14}	0.0	3.3797×10^4	[34]
5	$H + CO_2 \longleftrightarrow CO + OH$	1.6×10^{14}	0.0	1.32×10^4	[36]
6	$H + H_2O \longleftrightarrow H_2 + OH$	1.0×10^{10}	1.2	9.62×10^3	[36]
7	$H_2 + H \longleftrightarrow 2H + H$	8.5×10^{19}	−1.1	5.2335×10^4	[36]
8	$H_2 + H_2O \longleftrightarrow 2H + H_2O$	8.5×10^{19}	−1.1	5.2335×10^4	[36]
9	$H_2 + M \longleftrightarrow 2H + M$	9.0×10^{14}	0.0	4.840×10^4	H, H_2O = 0.0, [36]
10	$H_2 + O_2 \longleftrightarrow 2OH$	2.5×10^{12}	0.0	1.96×10^4	[36]
11	$H_2O + C \longleftrightarrow OH + H + C$	1.3×10^{21}	−1.0	6.0×10^4	[36]
12	$H_2O + H \longleftrightarrow OH + 2H$	1.3×10^{21}	−1.0	6.0×10^4	[36]
13	$H_2O + H_2O \longleftrightarrow OH + H + H_2O$	1.3×10^{21}	−1.0	6.0×10^4	[36]
14	$H_2O + M \longleftrightarrow OH + H + M$	1.3×10^{22}	−1.6	6.0×10^4	H, C, O, H_2O = 0.0, [36]
15	$H_2O + O \longleftrightarrow OH + H + O$	1.3×10^{21}	−1.0	6.0×10^4	[36]
16	$O + H_2 \longleftrightarrow OH + H$	3.9×10^4	2.7	3.15×10^3	[36]
17	$O + H_2O \longleftrightarrow 2OH$	3.4×10^{10}	1.0	8.6×10^3	[36]
18	$O_2 + M \longleftrightarrow 2O + M$	2.0×10^{21}	−1.5	5.936×10^4	H, C, O = 5.0, [37]
19	$OH + M \longleftrightarrow O + H + M$	2.4×10^{15}	0.0	5.0×10^4	[36]

Table 2 Engine plenum species mass fractions.

Species	Mass Fraction
H_2O	0.4009
CO_2	0.2698
H_2	0.0067
CO	0.2164
OH	0.0558
O_2	0.0413
O	0.0081
H	0.0010

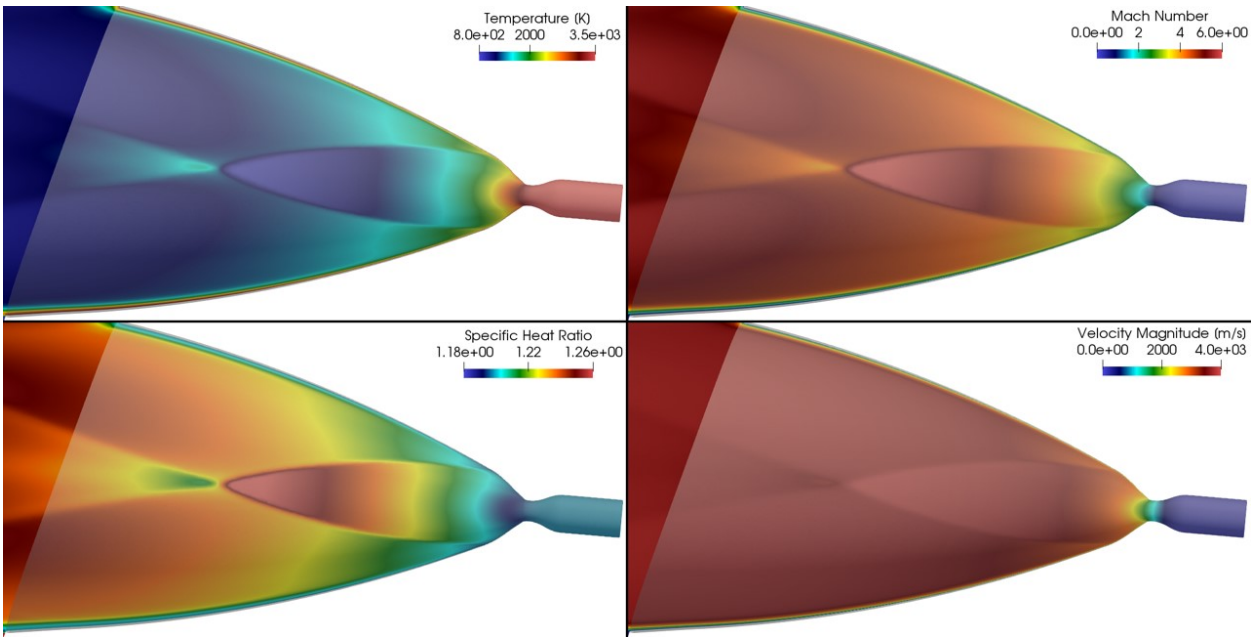


Fig. 6 Centerline slice of a nozzle at 60% throttle. Top Left: Temperature in Kelvin. Top Right: Mach number. Bottom Left: Specific heat ratio. Bottom Right: Velocity magnitude in m/s. The transparent gray surface indicates the scarfed nozzle walls.

A. Flowfield

Throttling conditions drastically affect flow features of interest. Figure 7, for example, depicts underexpanded and overexpanded perfect gas conditions. While the underexpanded nozzles lead to less aerodynamic drag on the vehicle due to larger aerodynamic interference, the thrust coefficient is higher than that for the overexpanded case, which leads to an overall larger deceleration force coefficient. The engineering question of interest is the impact of the more chaotic and unsteady flowfield on the stability of the vehicle during the powered flight phase of atmospheric entry.

Figures 8-9 show instantaneous contours at roughly one second of physical time on the nozzle Y-plane of various variables of interest. Detached bow shock standoff distances are similar between perfect gas air and reacting gas simulations at this physical point in time and are roughly two heatshield diameters in length. Plume shapes are also qualitatively similar between the reacting gas and perfect gas simulations. The specific heat ratio varies a substantial amount in the engines, plumes, and flow upstream of the vehicle; carbon dioxide in particular has significant thermodynamic property temperature variations around 200 to 1000 K. There are significant chemical reactions that occur in between the plumes and the bow shock; the mass fraction of hydroxl radical reaches values of 4%, which is quite large for supersonic combustion problems.

Figures 10 and 11 depict contours comparing the effects of throttling. The results are consistent with previous perfect gas campaigns. The underexpanded nozzles lead to significantly larger plumes, which obstruct pressure recovery on the heatshield. The mean bow shock standoff distances for the 80% and 60% throttle conditions are 45 and 18 meters, respectively. The underexpanded nozzles lead to a 2.5× larger bow shock standoff distance. The underexpanded nozzles also exhibit significantly more mixing than the overexpanded nozzles due to plume-plume interactions as shown in the hydroxl radical contours. Isosurfaces of H_2O mass fraction at two points in time are presented in Fig. 12.

The turbulent kinetic energy spectrum in Fig. 13 is shown to predict the same $-5/3$ power law in the inertial subrange as exhibited in canonical high Reynolds number incompressible turbulence. Mass fraction centerline and radial statistics are presented in Figs. 14-16. The 60% throttle composition near the centerline is the freestream composition due to the smaller overexpanded plumes. For the 80% throttle condition, the recirculation region caused by the plumes leads to substantial CO and H_2O at the stagnation point in addition to CO_2. The plume widths are approximately twice as large for the higher throttle case versus the lower throttle case.

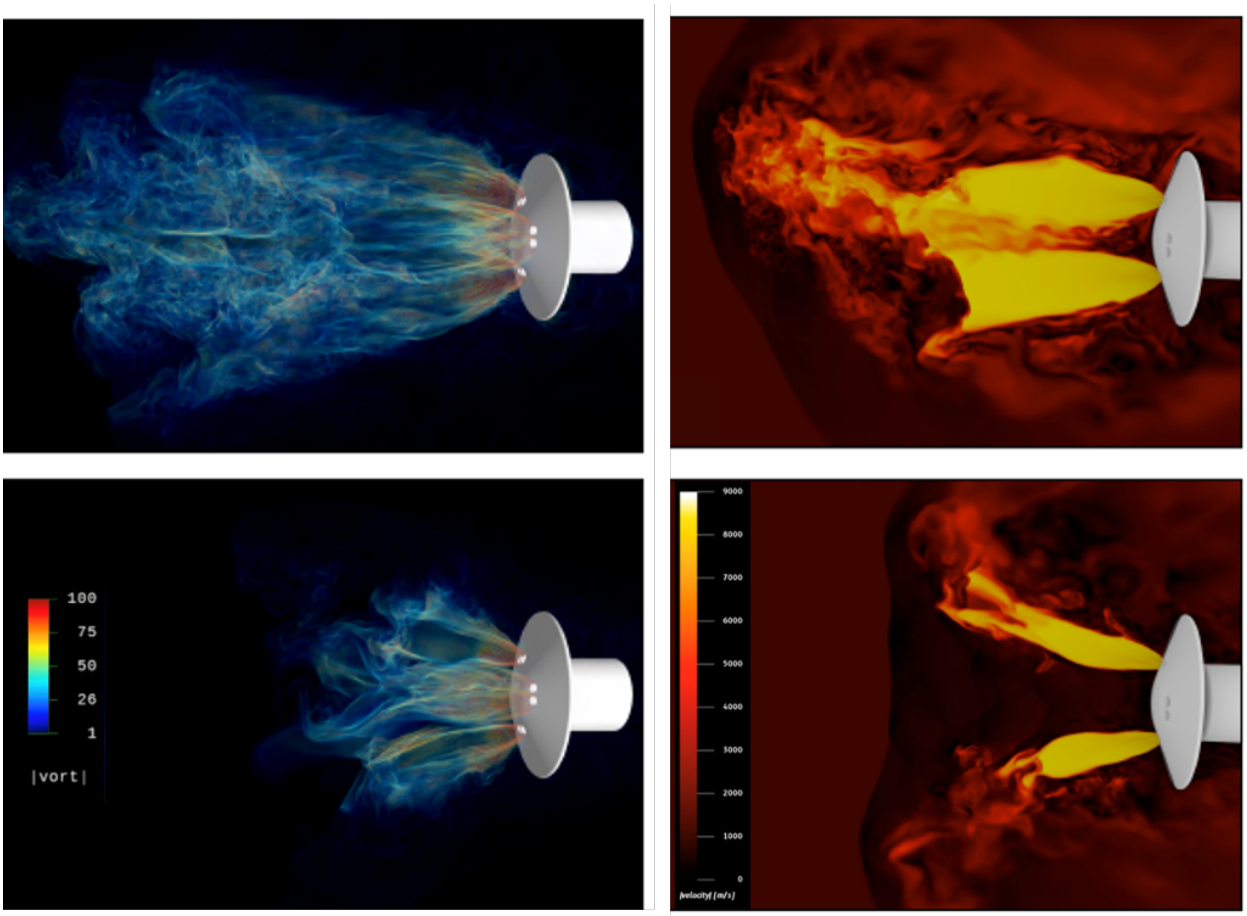
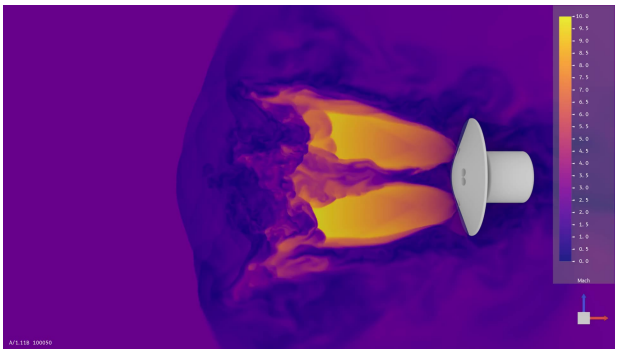
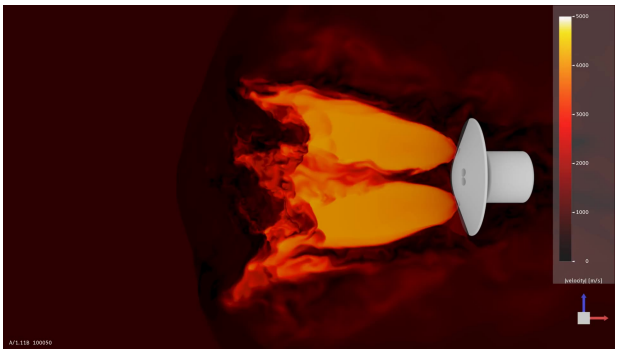


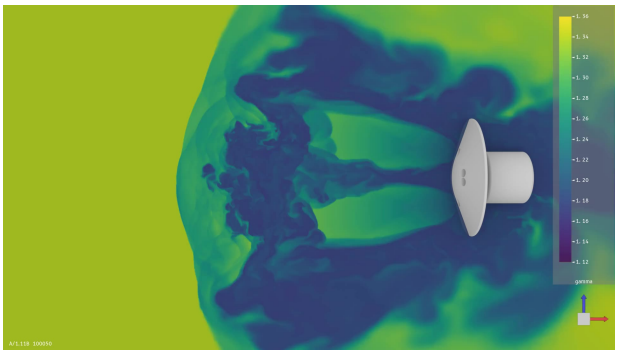
Fig. 7 Visualization of perfect gas simulations [12] using a grid consisting of 511 million points. Left: Instantaneous volume renderings of nondimensional vorticity magnitude. Right: Instantaneous velocity magnitude contours. Top figures correspond to underexpanded nozzle condition (80% throttle). Bottom figures correspond to overexpanded nozzle condition (60% throttle).



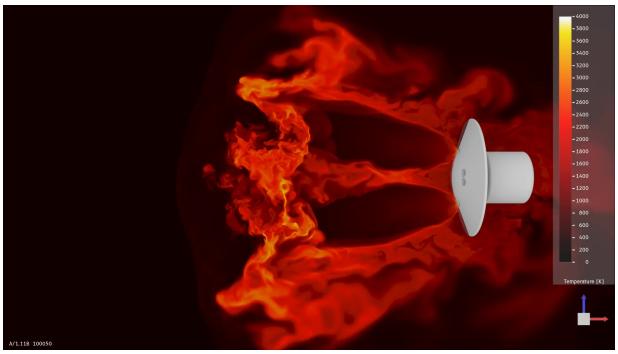
(a) Mach Number (Range 0.0 to 10.0)



(b) Velocity Magnitude [m/s] (Range 0.0 to 5000.0 [m/s])



(c) Specific Heat Ratio (Range 1.12 to 1.36)



(d) Temperature [K] (Range 0.0 to 4000.0 [K])

Fig. 8 Reacting gas instantaneous contours on a nozzle plane for the 80% throttle fine grid case.

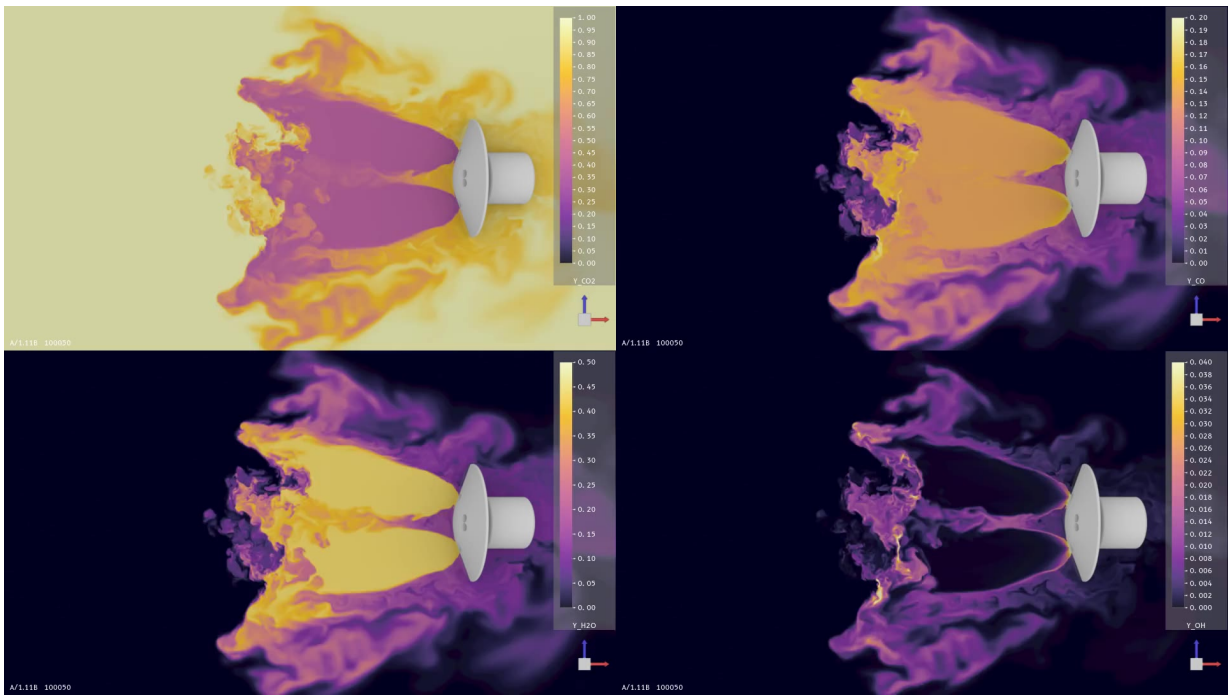


Fig. 9 Reacting gas instantaneous species mass fraction contours on a nozzle plane for the 80% throttle fine grid case. Top Left: CO_2 (Range 0.0 to 1.0). Top Right: CO (Range 0.0 to 0.2). Bottom Left: H_2O (Range 0.0 to 0.5). Bottom Right: OH (Range 0.0 to 0.04).

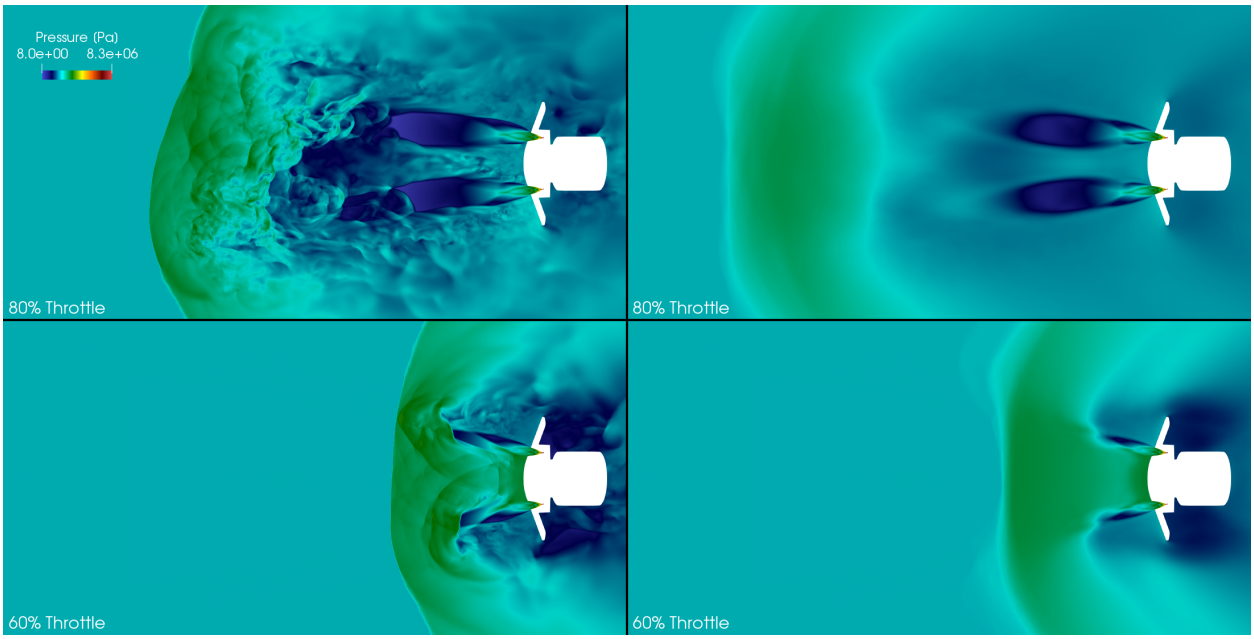


Fig. 10 Instantaneous (left) and mean (right) contours of pressure (scale in $\log_{10}$). Top: 80% throttle. Bottom: 60% throttle.

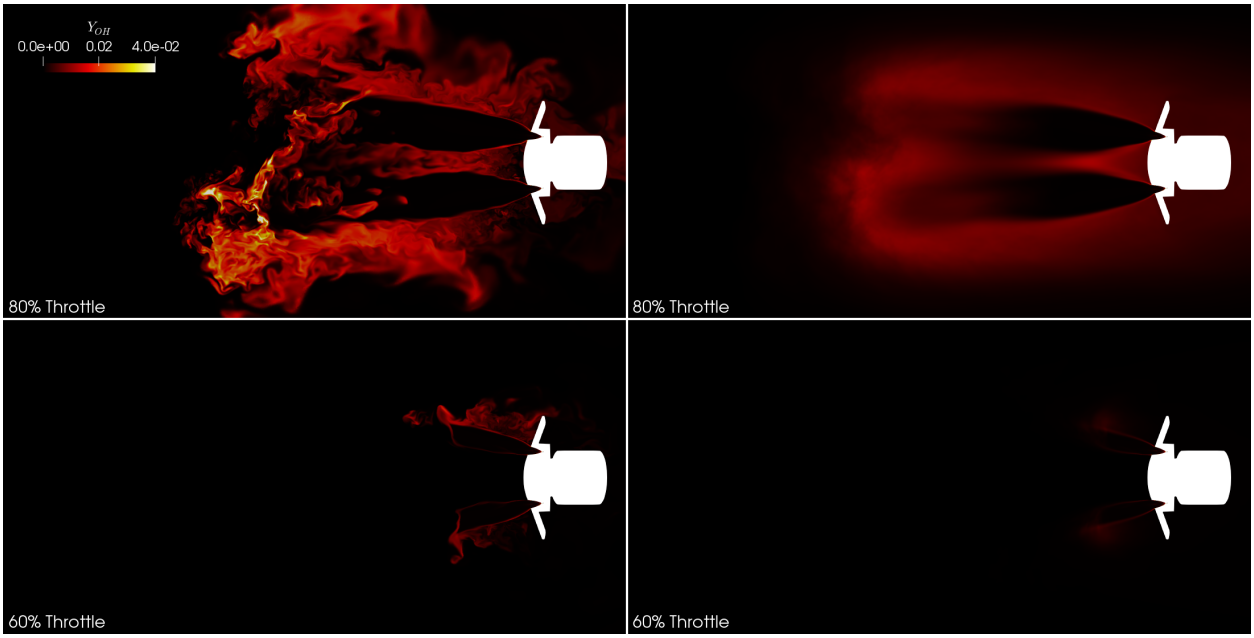
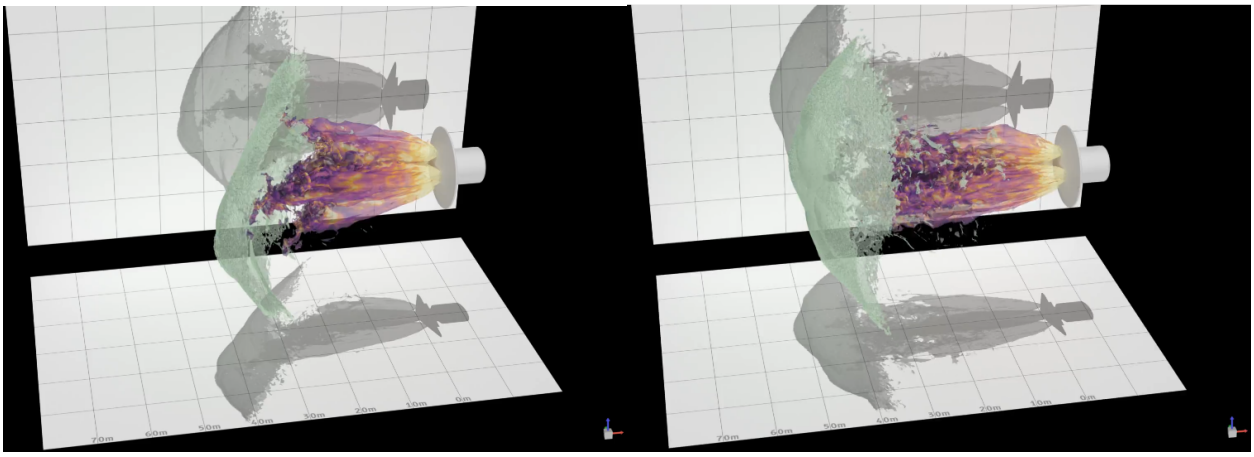


Fig. 11 Instantaneous (left) and mean (right) contours of hydroxl radical mass fraction. Top: 80% throttle. Bottom: 60% throttle.



(a) (b)

Fig. 12 Reacting gas H_2O mass fraction isosurfaces (40%) colored by vorticity magnitude with bow shock visualized by a shock sensor based on Ref. [38]. Visualizations are taken at 100,000 (a) and 300,000 (b) time steps. The Cartesian grid lines indicate a 10 meter spacing.

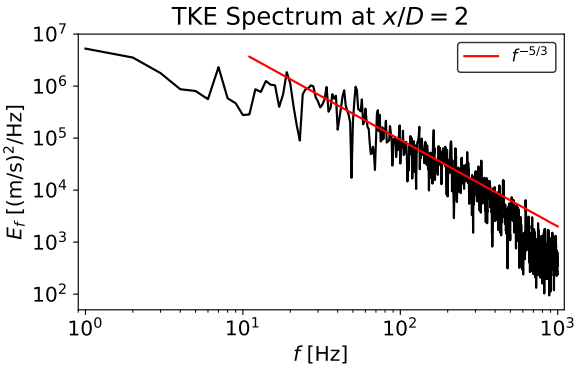
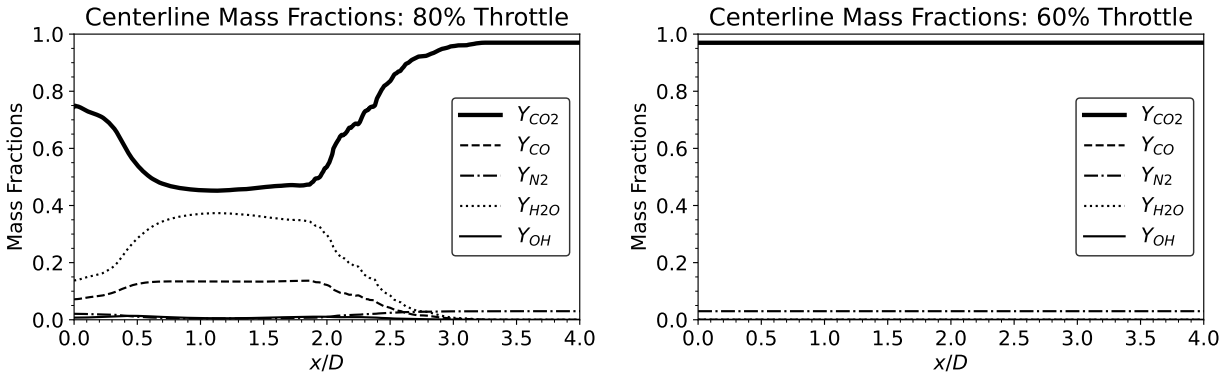
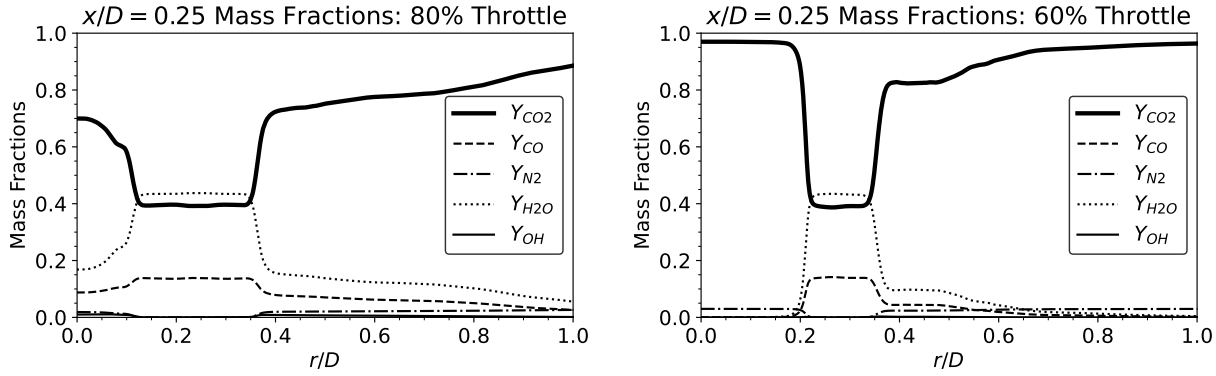


Fig. 13 Turbulent kinetic energy (TKE) spectrum based on the 80% throttle condition data at $x/D = 2$.



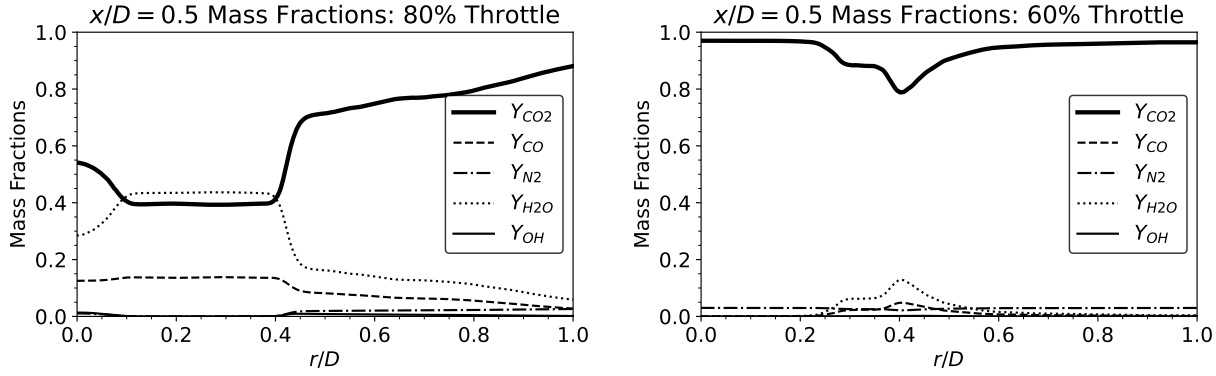
(a) (b)

Fig. 14 Reacting gas mean axial centerline mass fractions for 80% throttle (a) and 60% throttle (b).



(a) **(b)**

Fig. 15 Reacting gas mean radial mass fractions at $x/D = 0.25$ for 80% throttle (a) and 60% throttle (b).



(a) **(b)**

Fig. 16 Reacting gas mean radial mass fractions at $x/D = 0.5$ for 80% throttle (a) and 60% throttle (b).

B. Forces and Moments

The absence of pressure recovery on the heatshield for the 80% throttle case leads to significant effects on the forces and moments for the vehicle. This effect is readily visible in the mean surface pressure coefficient contour shown in Fig. 17. In addition to an absence of heatshield pressure recovery, the flowfield is less regular and exhibits asymmetric behavior (as shown in Fig. 12). Asymmetries have been predicted by previous simulations for past experiments [4], however, experimental diagnostics were not in place to discern or diagnose asymmetries confidently. Upcoming experiments using this Mars lander concept setup [13] will attempt to quantify asymmetries if they exist in the flowfields.

Means and standard deviations for the aerodynamic coefficients, including perfect gas results, are presented in Tables 3 and 4. Forces and moments, based on a body-fixed coordinate system, over time for the 139 million and 1.11 billion point grids are presented in Figs. 18-21. Note that the grids between the two throttle settings are identical; as such, the effective resolution for the 60% throttle condition versus the 80% throttle condition is lower since there are unused points upstream of the vehicle. The reference length and area are based on the heatshield diameter. The fine grid 80% throttle case is run additional time, but maintains the same averaging interval for forces and moments as the 139 million point grid, 80% throttle case for comparison. The results only show the aerodynamic contribution to the forces and moments. The axial thrust coefficients for 80% throttle and 60% throttle are 2.33 and 1.74, respectively. The thrust coefficients for the coarse and fine grids are within 0.6%. The reference asymmetric moment for the 80% throttle case in Table 3 differs between the reacting and perfect gas cases; asymmetry is observed in both perfect gas and reacting gas

cases, and the reference moment is the largest moment observed. In the case of perfect gas, an asymmetry is observed in the Y-plane nozzles, whereas the asymmetry is observed in the Z-plane nozzles for the reacting gas cases. The total axial aerodynamic coefficients between grid levels for reacting gas are comparable. The mean total axial aerodynamic coefficient for the underexpanded reacting gas cases is about 80% larger than the perfect gas case. The asymmetric moment is about 40% smaller in the mean than perfect gas, but about 70% larger in terms of standard deviation. Due to the asymmetry, the 80% throttle case was run further in time another 1.5 seconds. The asymmetry for the reacting gas case disappears after approximately three seconds of physical time (see Fig. 19). Another note is on the large transients exhibited by these flows. In reality, the time duration of the descent trajectory from Mach 2.4 to Mach 0.8 is approximately 30 seconds, with the vehicle continuously decelerating. Therefore, there are questions whether or not some flow features would have enough time to occur in reality.

The 60% throttle reacting gas total axial force aerodynamic coefficient is approximately 40% larger than the perfect gas counterpart. The difference is expected to be due to a slightly larger thrust coefficient for the perfect gas case, which is expected to produce larger plume structures that lead to less pressure recovery, and specific heat ratio differences. Chemical reactions upstream of the vehicle for the lower throttle setting are much less pronounced than the higher throttle setting, and are thus not expected to be the primary cause of the differences. No asymmetries were predicted for the lower throttle setting, which is consistent with previous perfect gas runs. The breakdown of the total coefficients is shown in Fig. 22. The current design methodologies for trajectory analysis incorporate substantially larger standard deviations than what are predicted here aerodynamically for improved robustness and to account for unknown and known uncertainties.

Table 3 Supersonic (M_∞ = 2.40) aerodynamic force and moment statistics for 80% throttle. Reference (denoted by ref) force and moment correspond to asymmetry direction.

Forebody Aerodynamic Coefficients

	C_A		C_{ref}		$C_{m,ref}$	
Case	μ	σ	μ	σ	μ	σ
Perfect Gas 143M	-0.0577	0.0425	-0.0001	0.0058	0.0001	0.0064
Perfect Gas 1.14B	-0.0783	0.0233	0.0134	0.0052	-0.0145	0.0057
Reacting Gas 139M	-0.0503	0.0542	-0.0087	0.0088	0.0095	0.0097
Reacting Gas 1.11B	-0.0402	0.0497	-0.0070	0.0087	0.0078	0.0095

Total Vehicle Aerodynamic Coefficients

	C_A		C_{ref}		$C_{m,ref}$	
Case	μ	σ	μ	σ	μ	σ
Perfect Gas 143M	0.0662	0.0415	-0.0002	0.0075	0.0003	0.0063
Perfect Gas 1.14B	0.0492	0.0512	0.0122	0.0066	-0.0152	0.0057
Reacting Gas 139M	0.0864	0.0536	0.0102	0.0102	0.0114	0.0094
Reacting Gas 1.11B	0.0912	0.0433	0.0084	0.0107	0.0093	0.0101

Table 4 Supersonic (M_∞ = 2.40) aerodynamic axial coefficient statistics for 60% throttle.

Total Vehicle Aerodynamic Coefficients

	C_A	
Case	μ	σ
Perfect Gas 143M	0.3540	0.0337
Perfect Gas 1.14B	0.2865	0.0501
Reacting Gas 139M	0.4538	0.0232
Reacting Gas 1.11B	0.3999	0.0353

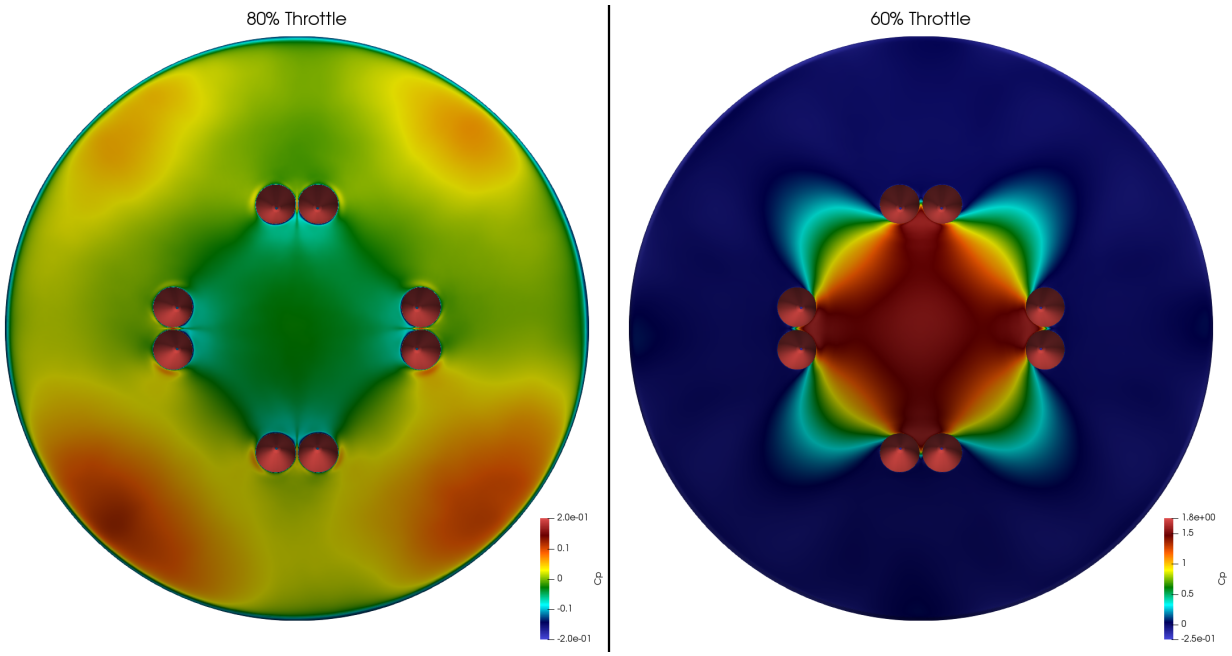


Fig. 17 Mean pressure coefficient on the heatshield. Left: 80% throttle. Right: 60% throttle.

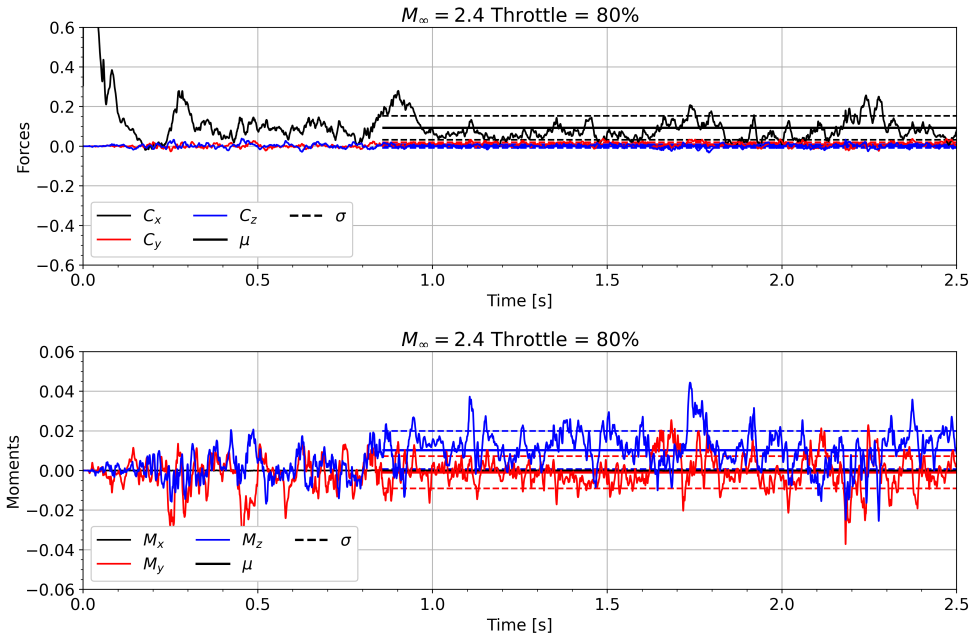


Fig. 18 Time histories, means, and standard deviations of total forces (top) and moments (bottom) for 139 million point grid at 80% throttle. Solid and dashed horizontal lines represent the mean and standard deviation, respectively.

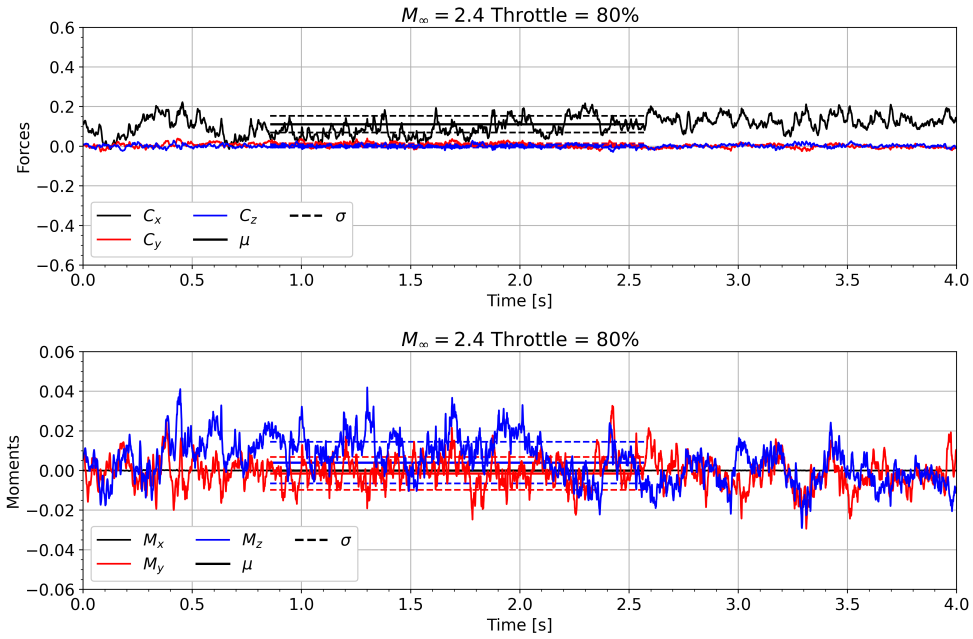


Fig. 19 Time histories, means, and standard deviations of total forces (top) and moments (bottom) for 1.11 billion point grid at 80% throttle. Solid and dashed horizontal lines represent the mean and standard deviation, respectively.

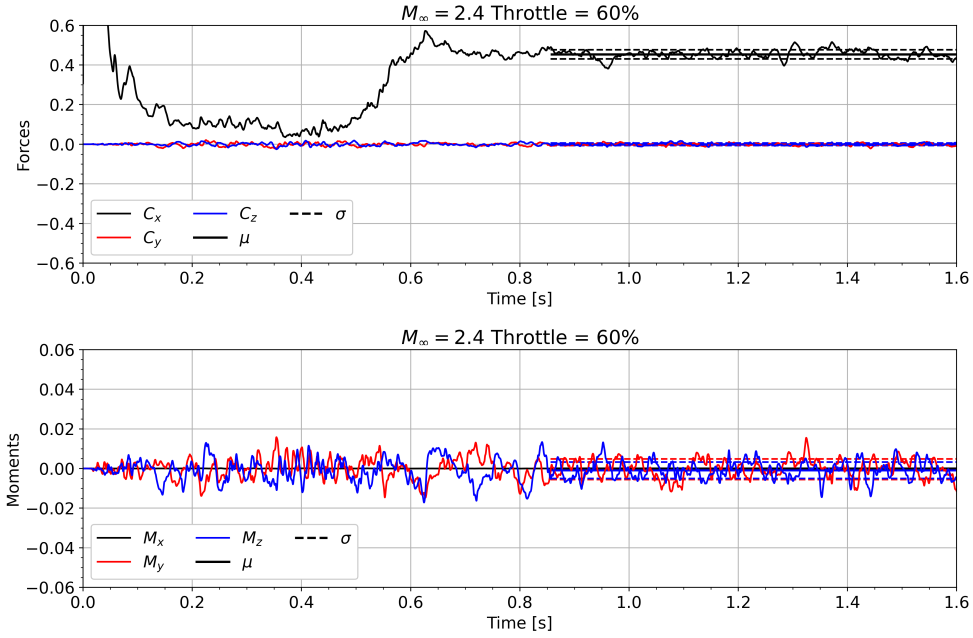


Fig. 20 Time histories, means, and standard deviations of total forces (top) and moments (bottom) for 139 million point grid at 60% throttle. Solid and dashed horizontal lines represent the mean and standard deviation, respectively.

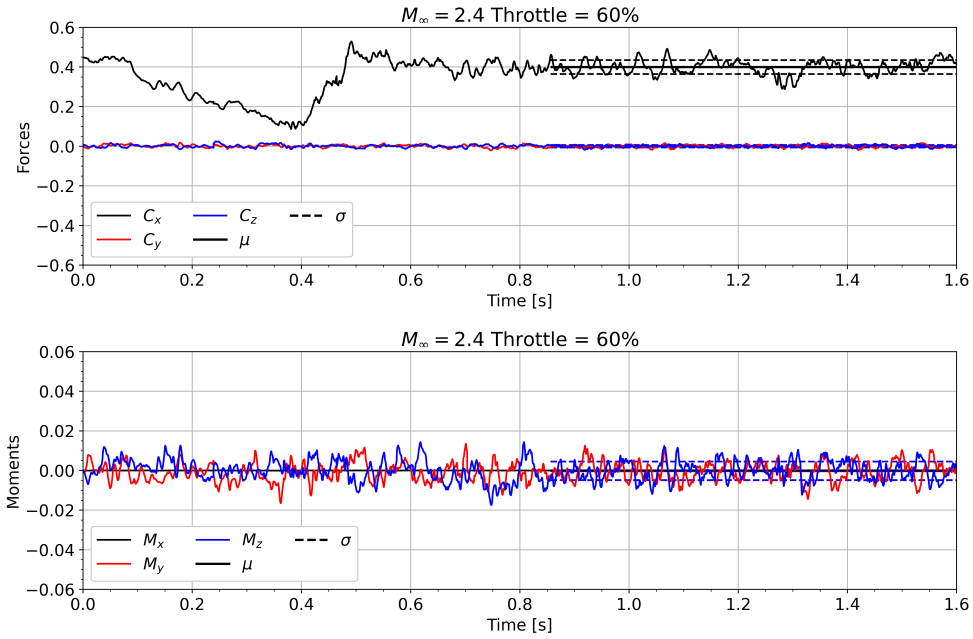


Fig. 21 Time histories, means, and standard deviations of total forces (top) and moments (bottom) for 1.11 billion point grid at 60% throttle. Solid and dashed horizontal lines represent the mean and standard deviation, respectively.

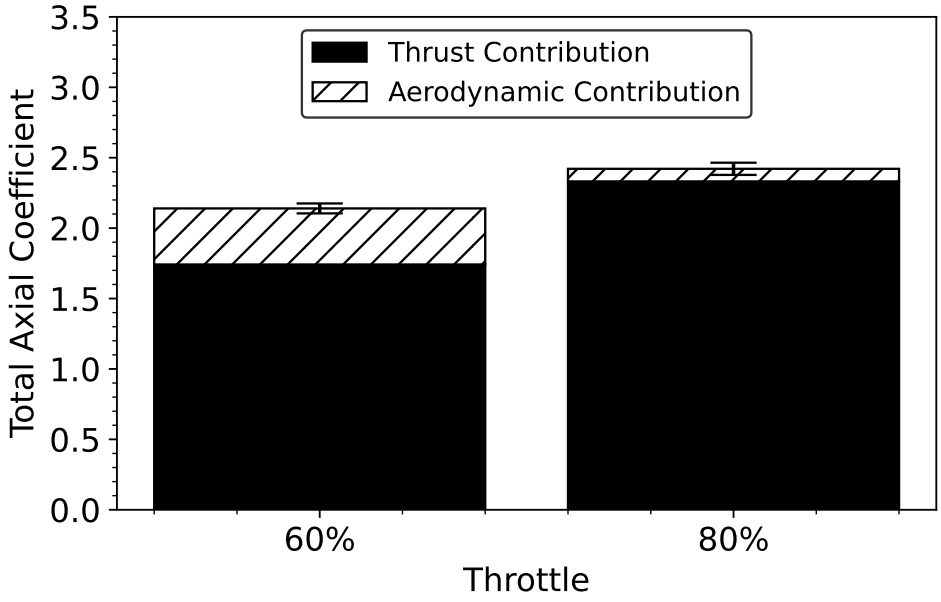


Fig. 22 Total axial coefficient breakdown including standard deviation due to aerodynamic contribution.

IV. Summary and Future Work

Chemically reacting, scale-resolving supersonic retropropulsion simulations have been carried out for a human-scale Mars lander concept. The simulations were each performed in a few days at scale on the Summit system at ORNL using thousands of NVIDIA Tesla V100 GPUs. The finite-rate chemistry simulations were carried out using a fully implicit temporal integration approach to enable reasonable time steps while fully resolving the wall to model turbulent effects (and eventually surface multiphysics) on the flowfield. The global maximum convective CFL is approximately 225 based on the plena wall conditions and of order one upstream of the vehicle. Because hybrid RANS-LES models are used, the flow near the wall is effectively RANS and diffusion dominated, which reduces the temporal error imposed by the larger convective time step.

Current results show qualitatively similar flow structures as compared to past perfect gas runs. Notably, for underexpanded plumes, asymmetries that last a few seconds are present in the flowfields, which lead to asymmetric aerodynamic moments on the vehicle. These asymmetries and dynamics would be difficult to predict with RANS. There are still open questions of whether or not asymmetries will be exhibited in the actual vehicle. Previous simulations and experiments have shown asymmetries. Upcoming experimental data investigating an air setup [13] will investigate potential asymmetries. For overexpanded plumes, pressure recovery occurs and the reacting gas simulations predict 40% larger axial force versus perfect gas, attributed to both a slightly larger thrust coefficient in the perfect gas case, which is expected to produce larger plume structures that lead to less pressure recovery, and specific heat ratio differences. Future work focusing on Mars vehicle design should, at a minimum, use pseudo-inert species. For underexpanded plumes, chemical reactions do occur upstream of the vehicle, enhanced by plume-plume interaction induced turbulence, and should be modeled at a minimum for thermal design if computational cost is prohibitive. The mean total axial coefficients for 60% and 80% throttle are 2.14 and 2.42, respectively. Overall, the aerodynamic axial coefficients are significantly smaller than the thrust coefficients, which is consistent with previous experimental and computational results for other vehicles and models. The aerodynamic contribution accounts for 19% and 4% of the total axial coefficient for 60% and 80% throttle conditions, respectively. There are thus questions regarding the engineering tradeoff of higher throttle at the expense of potential instability of the vehicle.

Future work includes algorithmic improvements to the solver including, but not limited to, alternative turbulence models, decoupled chemistry [39, 40], and improved lower-dissipation numerics. Experimental comparisons will also be made with upcoming experimental data [13]. Future experimental efforts regarding retropropulsion should attempt to investigate the effects of chemistry on model problems that are representative of future Mars lander concepts for validation.

Appendix

A. Supersonic Retropropulsion Flow for a Single Engine Vehicle

A perfect gas experimental configuration is investigated to determine turbulence model impacts on surface pressure. The perfect gas experiment has a freestream Mach number and unit Reynolds number of $M_\infty = 4.6$ and $Re_\infty = 5 \times 10^6$ 1/m, respectively. The diameter of the 70-degree sphere-cone is 5 inches, and the nozzle exit diameter is 0.5 inches. The area ratio of the conical nozzle exit-to-throat is 4:1. The nozzle total pressure and total temperature with respect to freestream conditions are $p_0/p_\infty = 7724.3$ and $T_0/T_\infty = 5.34$, respectively. Further details including experimental schematics are presented in Ref. [5].

For this single-nozzle study, grids are generated with Capstone [41]. Figure 23 shows a centerline slice of the 3-D grid. There is a fine cylindrical nozzle source with a spacing of 0.5 mm. The spherical source just outside the nozzle exit and surface spacing are 2 mm. The sphere encasing the rest of the vehicle uses a spacing of 5 mm. A y^+ of 1 is used to size the first prismatic boundary layer node off the surface. The grid consists of 15,248,710 points, 78,789,184 tetrahedra, and 4,198,366 prisms. Two finer grids are generated for a grid refinement study by increasing the volume and surface spacing resolution sources (fixing the boundary layer properties) by 25% and 50%, leading to grids with approximately double and triple the number of points in the original grid, respectively. The spacing to nozzle diameter ratio for the finest grid is comparable to the Mars lander concept 139 million point grid.

The no-slip walls are modeled as adiabatic. The equations are integrated in time using two-step backward difference (BDF2) time integration with a physical time step of 1 μs. Three subiterations are used for each time step, leading to nominally two orders of magnitude reduction in all of the residuals. Turbulence is modeled using three different models: SA DES [11], SA-Catris DES [29], and URANS (with SST [42]).

Results are presented in Figs. 24-26. The original grid is shown to be adequate for RANS in Fig. 25 and is also

comparable to previous computational investigations [4], and is thus the grid used for the unsteady simulations. The nominal thrust coefficient is 2.0, with all simulations predicting values within 2% of nominal. Mean pressure coefficient results agree favorably with experimental data. The nose surface pressure is slightly overpredicted for the 12 and 20 degree angles of attack for SA DES and SA-Catris DES and is slighty underpredicted for URANS. Drag coefficient standard deviation in time is also similar for SA DES and SA-Catris DES, with URANS results not as unsteady due to higher turbulent viscosity. Overall, the SA-Catris DES variant leads to slightly improved experimental prediction versus SA DES. Results also compare favorably to past investigations using OVERFLOW, DPLR, and FUN3D [4].

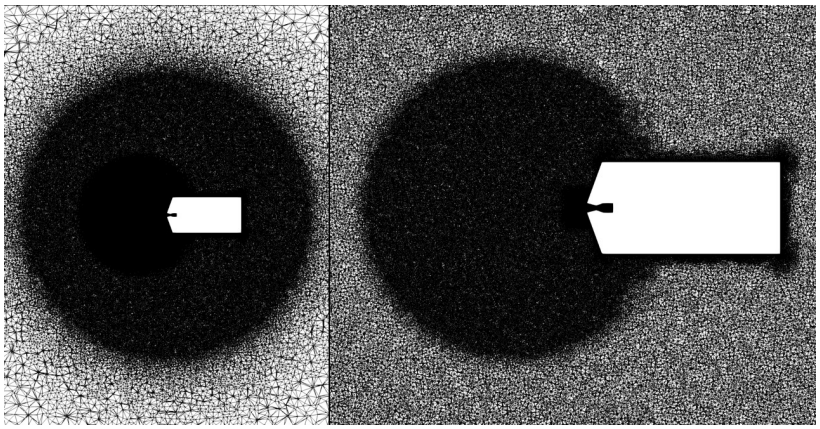


Fig. 23 Y-plane center slice of the single nozzle grid of 15 million points.

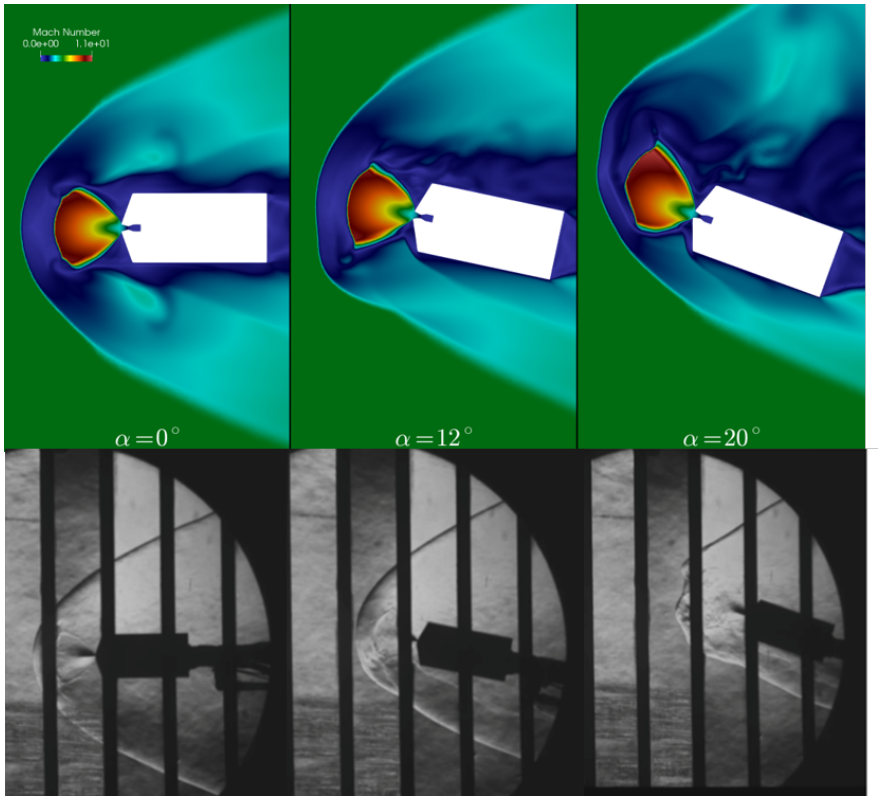


Fig. 24 Top: SA-Catris DES Mach number contours at various time snapshots. Bottom: Experimental schlieren of the same runs [5]. Angles of attack from left to right are 0, 12, and 20 degrees.

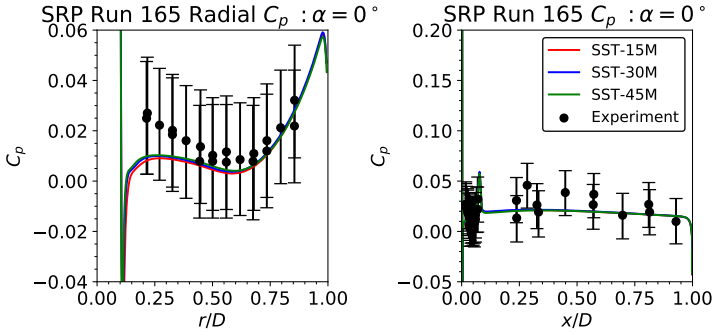


Fig. 25 Pressure coefficients for grid refinement study using SST turbulence model.

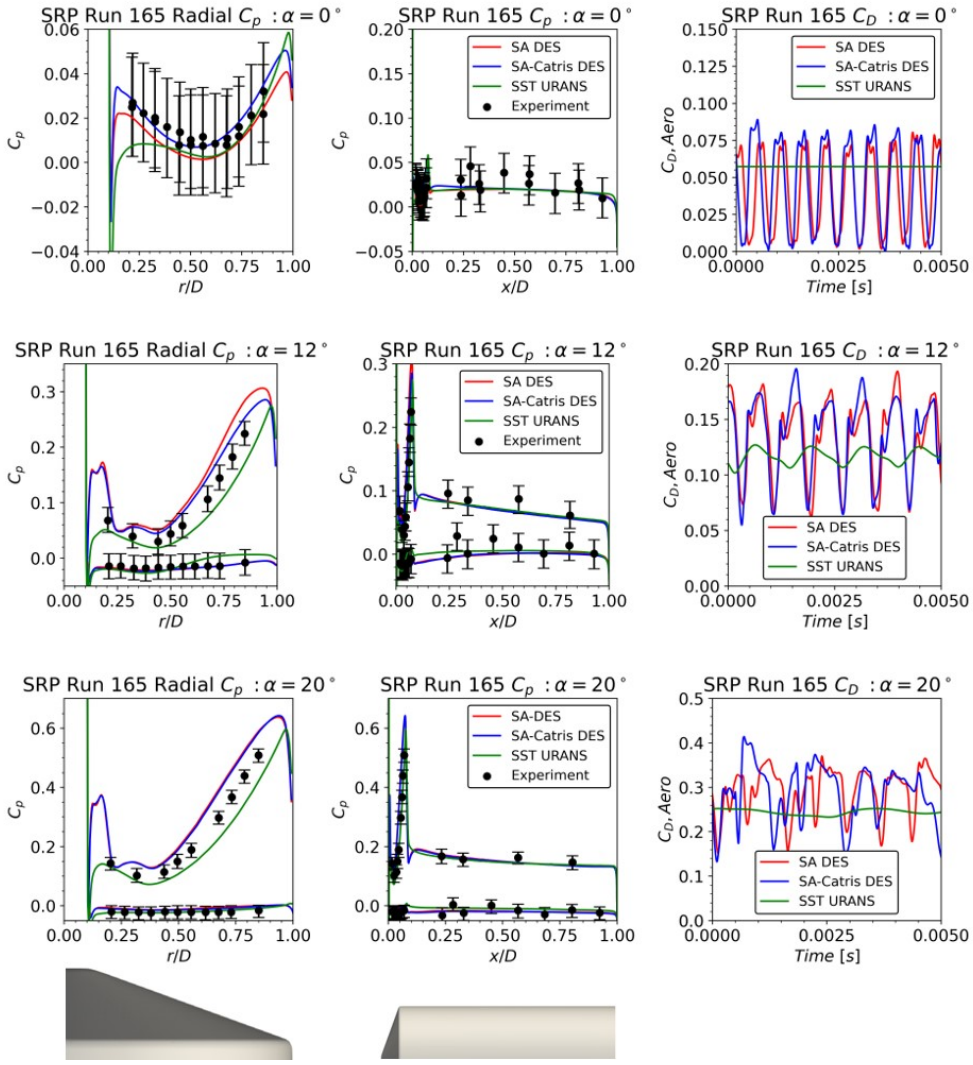


Fig. 26 Pressure coefficient plots of the perfect gas simulations along the radial nose and axial body. Drag aerodynamic coefficients versus time are also presented. Rows correspond to a single angle of attack.

Acknowledgments

This research was sponsored by the NASA Langley Research Center CIF/IRAD program and the NASA Transformational Tools and Technologies (TTT) Project of the Transformative Aeronautics Concepts Program under the Aeronautics Research Mission Directorate. The authors would like to thank the Department of Defense High Performance Computing Modernization Program, NVIDIA, and Sameer Shende of the University of Oregon. This research used resources of the Oak Ridge Leadership Computing Facility at the Oak Ridge National Laboratory, which is supported by the Office of Science of the U.S. Department of Energy under Contract No. DE-AC05-00OR22725.

References

[1] Dwyer-Cianciolo, A. M., Polsgrove, T., Sostaric, R. R., Edquist, K. T., Korzun, A. M., and Garcia, J. A., "Human Mars Entry, Descent, and Landing Architecture Study: Phase 3 Summary," *AIAA Paper 2021-1509*, 2021.

[2] Korzun, A. M., Cruz, J. R., and Braun, R. D., "A Survey of Supersonic Retropropulsion Technology for Mars Entry, Descent, and Landing," *Journal of Spacecraft and Rockets*, Vol. 46, No. 5, 2009, pp. 929–937.

[3] Trumble, K., "An Initial Assessment of Navier-Stokes Codes Applied to Supersonic Retro-Propulsion," *AIAA Paper 2010-5047*, 2010.

[4] Schauerhamer, D., Trumble, K., Kleb, W., Carlson, J.-R., and Edquist, K., "Continuing Validation of Computational Fluid Dynamics for Supersonic Retropropulsion," *AIAA Paper 2012-864*, 2012.

[5] Berry, S. A., and Rhode, M. N., "Supersonic Retropropulsion Test 1853 in NASA LaRC Unitary Plan Wind Tunnel Test Section 2," *NASA/TP-2014-218256*, 2014.

[6] Alkandry, H., "Aerodynamic Interactions of Propulsive Deceleration and Reaction Control System Jets on Mars-Entry Aeroshells." Ph.D. thesis, University of Michigan, 2012.

[7] Raghunandan, P., Hill, J., Ruffin, S. M., and Muppidi, S., "Aerothermal and Aerodynamic Characterization of Reacting Jets for Supersonic Retropropulsive Missions to Mars," *AIAA Paper 2018-3766*, 2018.

[8] Edquist, K. T., Korzun, A. M., Bibb, K., Schauerhamer, D. G., Ma, E. C., McCloud, P. L., Palmer, G. E., and Monk, J. D., "Comparison of Navier-Stokes Flow Solvers to Falcon 9 Supersonic Retropropulsion Flight Data," *AIAA Paper 2017-5296*, 2017.

[9] Ecker, T., Zilker, F., Dumont, E., Karl, S., and Hannemann, K., "Aerothermal Analysis of Reusable Launcher Systems During Retro-Propulsion Reentry and Landing," *Space Propulsion Conference Paper 2018-40*, 2018.

[10] Ecker, T., Karl, S., Dumont, E., Stappert, S., and Krause, D., "Numerical Study on the Thermal Loads During a Supersonic Rocket Retropropulsion Maneuver," *Journal of Spacecraft and Rockets*, Vol. 57, No. 1, 2020, pp. 131–146.

[11] Spalart, P. R., "Comments on the Feasibility of LES for Wings, and on a Hybrid RANS/LES Approach," *Proceedings of First AFOSR International Conference on DNS/LES*, Greyden Press, 1997, pp. 137–147.

[12] Korzun, A. M., Nielsen, E., Walden, A., Jones, W., Carlson, J.-R., Moran, P., Henze, C., and Sandstrom, T., "Computational Investigation of Retropropulsion Operating Environments with a Massively Parallel Detached Eddy Simulation Approach," *AIAA Paper 2020-4228*, 2020.

[13] Edquist, K. T., Korzun, A. M., Kleb, W. L., Hawke, V., Rizk, Y. M., Olsen, M. E., and Canabal, F., "Model Design and Pre-Test CFD Analysis for a Supersonic Retropropulsion Wind Tunnel Test," *AIAA Paper 2020-2230*, 2020.

[14] ORNL, "Summit," `https://www.olcf.ornl.gov/olcf-resources/compute-systems/summit`, 2020. Last Accessed November 1, 2021.

[15] Stevens, R., Ramprakash, J., Messina, P., Papka, M., and Riley, K., "Aurora: Argonne's Next-Generation Exascale Supercomputer," Tech. rep., Argonne National Laboratory, 2019.

[16] ORNL, "Frontier," `https://www.olcf.ornl.gov/frontier`, 2020. Last Accessed November 1, 2021.

[17] Thomas, J., "El Capitan," `https://www.llnl.gov/news/llnl-and-hpe-partner-amd-el-capitan-projected-worlds-fastest-supercomputer`, 2020. Last Accessed November 1, 2021.

[18] Slotnick, J., Khodadoust, A., Alonso, J., Darmofal, D., Gropp, W., Lurie, E., and Mavriplis, D., "CFD Vision 2030 Study: A Path to Revolutionary Computational Aerosciences," *NASA CR-2014-218178*, 2014.

[19] Schuster, D. M., "CFD2030 Grand Challenge: CFD-in-the-Loop Monte Carlo Simulation for Space Vehicle Design," *AIAA SciTech Forum 2021-0957*, 2021.

[20] Nastac, G., Walden, A., Nielsen, E. J., and Frendi, A., "Implicit Thermochemical Nonequilibrium Flow Simulations on Unstructured Grids using GPUs," *AIAA Paper 2021-0159*, 2021.

[21] Urzay, J., "Supersonic Combustion in Air-Breathing Propulsion Systems for Hypersonic Flight," *Annual Review of Fluid Mechanics*, Vol. 50, 2018, pp. 593–627.

[22] Korzun, A., Nastac, G., Walden, A., Nielsen, E. J., Jones, W., and Moran, P., "Application of a Detached Eddy Simulation Approach with Finite-Rate Chemistry to Mars-Relevant Retropropulsion Operating Environments," *AIAA SciTech 2022 Forum*, 2022.

[23] McBride, B. J., Gordon, S., and Reno, M. A., "Coefficients for Calculating Thermodynamic and Transport Properties of Individual Species," *NASA TM 4513*, 1993.

[24] Gnoffo, P. A., Gupta, R. N., and Shinn, J. L., *Conservation Equations and Physical Models for Hypersonic Air Flows in Thermal and Chemical Nonequilibrium*, NASA TP 2867, 1989.

[25] Biedron, R. T., Carlson, J.-R., Derlaga, J. M., Gnoffo, P. A., Hammond, D. P., Jones, W. T., Kleb, B., Lee-Rausch, E. M., Nielsen, E. J., Park, M. A., et al., *FUN3D Manual: 13.7*, NASA TM 20205010139, 2020.

[26] Roe, P. L., "Approximate Riemann Solvers, Parameter Vectors, and Difference Schemes," *Journal of Computational Physics*, Vol. 43, No. 2, 1981, pp. 357–372.

[27] Burg, C., "Higher Order Variable Extrapolation For Unstructured Finite Volume RANS Flow Solvers," *AIAA Paper 2005-4999*, 2005.

[28] Van Leer, B., "Towards the Ultimate Conservative Difference Scheme. V. A Second-Order Sequel to Godunov's Method," *Journal of Computational Physics*, Vol. 32, No. 1, 1979, pp. 101–136.

[29] Catris, S., and Aupoix, B., "Density Corrections for Turbulence models," *Aerospace Science and Technology*, Vol. 4, No. 1, 2000, pp. 1–11.

[30] Korzun, A. M., Nielsen, E. J., Walden, A. C., Jones, W. T., Carlson, J.-R., Moran, P. J., Henze, C. E., and Sandstrom, T. A., "Effects of Spatial Resolution on Retropropulsion Aerodynamics in an Atmospheric Environment," *AIAA Paper 2020-1749*, 2020.

[31] Jones, W., "GridEx-An Integrated Grid Generation Package for CFD," *AIAA Paper 2003-4129*, 2003.

[32] Marcum, D., and Gaither, J., "Mixed Element Type Unstructured Grid Generation for Viscous Flow Applications," *AIAA Paper 1999-3252*, 1999.

[33] Biedron, R., and Thomas, J., "Recent Enhancements to the FUN3D Flow Solver for Moving-Mesh Applications," *AIAA Paper 2009-1360*, 2009.

[34] Johnston, C., and Brandis, A., "Modeling of Nonequilibrium CO Fourth-Positive and CN Violet Emission in CO2–N2 Gases," *Journal of Quantitative Spectroscopy and Radiative Transfer*, Vol. 149, 2014, pp. 303–317.

[35] Park, C., Howe, J. T., Jaffe, R. L., and Candler, G. V., "Review of Chemical-Kinetic Problems of Future NASA Missions. II-Mars Entries," *Journal of Thermophysics and Heat Transfer*, Vol. 8, No. 1, 1994, pp. 9–23.

[36] Fujita, K., Yamada, T., and Ishii, N., "Impact of Ablation Gas Kinetics on Hyperbolic Entry Radiative Heating," *AIAA Paper 2006-1185*, 2006.

[37] Park, C., *Nonequilibrium Hypersonic Aerothermodynamics*, Wiley, 1989.

[38] Nastac, G., Tramel, R., and Nielsen, E. J., "Improved Heat Transfer Prediction for High-Speed Flows over Blunt Bodies using Adaptive Mixed-Element Unstructured Grids," *AIAA SciTech 2022 Forum*, 2022.

[39] Candler, G. V., Subbareddy, P. K., and Nompelis, I., "Decoupled Implicit Method for Aerothermodynamics and Reacting Flows," *AIAA Journal*, Vol. 51, No. 5, 2013, pp. 1245–1254.

[40] Thompson, K. B., and Gnoffo, P. A., "A Decoupled Method for the Roe FDS Scheme in the Reacting Gas Path of FUN3D," *AIAA Paper 2016-2062*, 2016.

[41] Dey, S., Aubry, R. M., Karamete, B. K., and Mestreau, E. L., "Capstone: A Geometry-Centric Platform to Enable Physics-Based Simulation and System Design," *Computing in Science & Engineering*, Vol. 18, No. 1, 2015, pp. 32–39.

[42] Menter, F. R., "Two-Equation Eddy-Viscosity Turbulence Models for Engineering Applications," *AIAA Journal*, Vol. 32, No. 8, 1994, pp. 1598–1605.